A SIMPLIFIED THREE-PHASE MODEL OF EQUIAXED SOLIDIFICATION FOR THE PREDICTION OF MICROSTRUCTURE AND MACROSEGREGATION IN CASTINGS

Knut Omdal Tveito[1], Akash Pakanati[1], Mohammed M'Hamdi[1,2], Hervé Combeau[3,4], Miha Založnik[3,4]

[1] Dept. of Materials Technology, NTNU, N-7491 Trondheim, Norway
[2] SINTEF Materials and Chemistry, N-0314 Oslo, Norway
[3] Institut Jean Lamour, CNRS – Université de Lorraine, 2 allée André Guinier, BP 50840, F-54011 Nancy CEDEX, France
[4] Laboratory of Excellence on Design of Alloy Metals for low-mAss Structures ('DAMAS'), Université de Lorraine, France

* Corresponding author: Akash Pakanati (akash.pakanati@ntnu.no)

Abstract

Macrosegregation is a result of the interplay of various transport mechanisms, including natural convection, solidification shrinkage, and grain motion. Experimental observations also indicate the impact of grain morphology, ranging from dendritic to globular, on macrosegregation formation. To avoid the complexity arising due to modelling of an equiaxed dendritic grain, we present the development of a simplified three-phase, multiscale equiaxed dendritic solidification model based on the volume averaging method, that accounts for the above-mentioned transport phenomena. The validity of the model is assessed by comparing it to the full three phase model without simplifications. It is then applied to qualitatively analyze the impact of grain morphology on macrosegregation formation in an industrial scale direct chill (DC) cast aluminium alloy ingot.

Keywords: Solidification, Dendritic growth, DC casting, Macrosegregation

1. Introduction

Macrosegregation is a severe defect in DC casting of aluminium alloys. It refers to the solute inhomogeneity at the scale of the casting and is a direct result of microsegregation at the scale of the dendrite arm spacing. As the solubility of solute elements in the solid phase is lower than in the liquid, solidification is accompanied by rejection of the solutes into the liquid phase. Rejected solutes are transported due to the relative motion of solid and liquid phases, which eventually results in macrosegregation. Different mechanisms contribute to this relative motion in DC casting: solidification shrinkage induced flow, thermal and solutal natural convection, movement of the equiaxed grains and thermally induced deformations of the mushy zone. For a detailed description of these mechanisms, the reader is referred to Ref[1].

Several modelling attempts have been made to describe macrosegregation formation[2–4]. Many researchers attempted to numerically analyze the formation of macrosegregation in DC casting[5–7] using models based on the volume averaging method[8]. It is commonly agreed that accounting for grain motion is important in order to provide a sound description of macrosegregation formation. Reddy and Beckermann[9] made the first attempts to account for the impact of grain motion on macrosegregation formation assuming spherical grains. In DC casting, both globular and dendritic grain morphologies can be observed[10,11]. Simplifications of the dendritic morphology by considering globular grains in numerical models resulted in large discrepancies between model predictions and experiments[12]. Rappaz and Thévoz[13–15] were the first to propose a multiscale diffusion model to numerically simulate equiaxed dendritic solidification in castings accounting for grain morphology. To accurately describe the growth of dendritic grains they introduced the notion of the dendrite envelope and of three hydrodynamic phases – solid, intragranular (also called interdendritic) liquid and extragranular (also called extradendritic) liquid. Wang and Beckermann[16–18] introduced these ideas into volume-averaging multiphase models

and proposed the first model of equiaxed dendritic solidification that accounted for grain morphology in the presence of convection and grain motion. Wu and Ludwig[19] proposed a 5-phase solidification model by adding two hydrodynamic phases to the three thermodynamic phases. Vreeman et al[20] proposed a numerical model accounting for grain motion to predict macrosegregation formation in DC cast aluminium alloys and applied the model to conduct a study on DC cast billets with Al-Mg and Al-Cu[21]. Solidification modelling with grain motion introduces complexities due to coupled macroscopic transport phenomena and microscopic growth kinetics. To overcome this issue, Založnik and Combeau[22] proposed a splitting scheme for two-phase solidification models. In this scheme the contributions due to macroscopic transport and grain growth kinetics are solved in two separate stages. Their model was further extended to predict macrosegregation formation in DC casting but the morphology of the grain was limited to globular equiaxed grains[23].

Although a a more detailed description of the grain morphology is possible by introducing additional phases, the complexity of the model also increases due to the larger number of transport equations. To avoid this pitfall, a simplification of a three-phase solidification model for the growth kinetics of dendritic equiaxed grains is proposed in this paper. The simplification allows us to integrate the three-phase grain growth model into the framework of two-phase macroscopic transport equations. This solidification model is then solved with the splitting scheme by Založnik and Combeau[22]. First, a validation study is conducted by comparing this simplified three-phase model with the full three-phase model. Subsequently, a preliminary application of the model to study the impact of grain morphology at the process scale is made by applying the model to predict macrosegregation formation in an industrial scale DC cast aluminium ingot in a qualitative manner.

2. Model Description

The volume-averaged model of dendritic solidification is described in the following subsections. We first describe the general three-phase approach to dendritic equiaxed solidification, which is based on the model proposed by Wang and Beckermann[16]. We then go through the conservation equations and derive the complete dendritic model. Starting from the complete model we introduce several simplifying assumptions. These assumptions lead us to an approximate model that is formulated in a similar way and with the same number of equations as a two-phase model, although it retains the concepts and the physical ingredients of the three-phase model. We then carry out a validation study of the approximate model by comparing the most critical model outputs to the complete model. Note that only equiaxed solidification is considered here, but that the model can be combined with a model of columnar solidification.

2.1. Three-phase approach to dendritic equiaxed solidification

Figure 1 shows an illustration of a representative elementary volume (REV) in the mushy zone. The REV contains solid in form of equiaxed dendritic grains and liquid. The morphology of the solid grains is characterized by the primary dendrite arms, with its tips marking the extremities of the grain and the secondary and higher-order dendrite arms growing out of the primary dendrites. The growth of the grains is controlled by solute rejection from the growing solid into the surrounding liquid. While solute transport at the scale of the REV is determinant for the growth, all phases in the REV can be considered to be thermally in equilibrium due to the high Lewis numbers of metals ($Le \sim 10^4$ for Al alloys). The extraction of sensible and latent heat is controlled by macroscopic heat transfer processes. Due to the intricate morphology, the solute transport from the growing grain into the surrounding liquid is controlled by diffusion and convection at multiple length scales. At the smallest scale, there is diffusion in the boundary layer around the dendrite tips, which controls the tip growth. In the liquid between the branches of the dendritic structure the solute transport is mainly by diffusion and the diffusion length is characterized by the spacing of the secondary dendrite arms. Outside the dendritic structure the convection and diffusion are characterized by the grain size and by the distance between the grains. To model dendritic solidification all these length scales need to be considered in the model. In a volume-

averaging framework all local quantities (grain size, growth velocity, concentrations, etc.) are of course considered as spatial averages over the REV.

To model the dendritic solidification, three separate regions (or *hydrodynamic phases*) are considered: i) the solid phase (denoted *s*), *ii)* the intragranular liquid (denoted *d*) and *iii*) the extragranular liquid (denoted *e*). It should be noted that the intra- and extragranular liquid are same as the inter- and extradendritic liquid described in Ref[16]. The intra- and extragranular liquids are separated by the grain envelope, i.e. a smooth surface enveloping the entire dendritic structure. While the two liquids are indeed the same thermodynamic phase, they are modeled separately in order to describe the different scales of diffusion arising from the dendritic morphology in a volume-averaged framework.

Before deriving the dendritic model, its main assumptions are summarized:

- Local thermal equilibrium.
- Thermodynamic equilibrium in the intragranular liquid due to fast diffusion at the scale of the secondary dendrite arm spacing.
- The densities of the intra- and extragranular liquids are identical and equal to the average liquid density ($\rho_d = \rho_e = \rho_l$).
- The diffusion coefficients of the solid and liquid phases are assumed constant, but unequal.
- Macroscopic diffusion in solid and liquid phases is neglected.

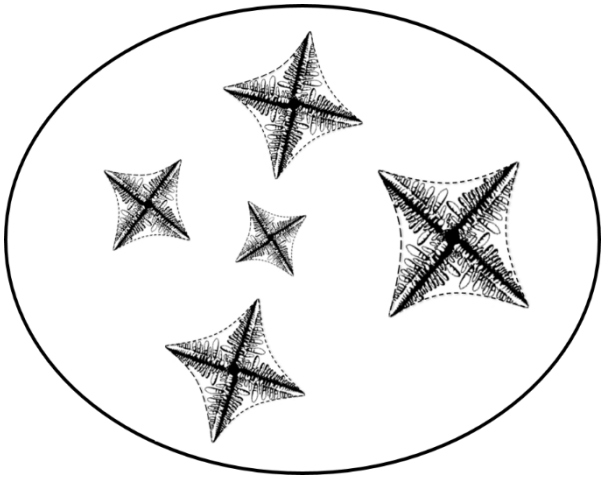

Figure 1: Representative Elementary Volume

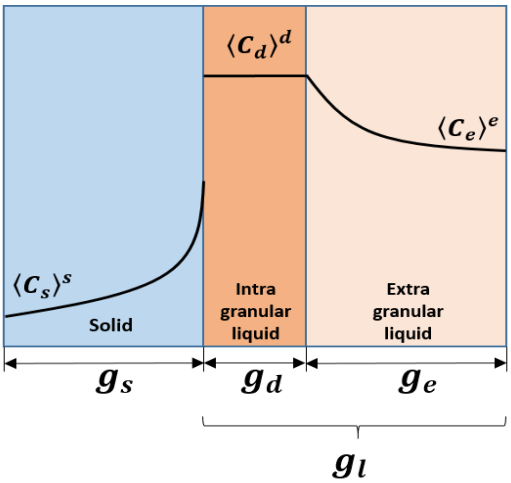

Figure 2: 1D Schematics of the three-phase model

2.2. Volume-averaged mass conservation equations

The complete derivation of the volume-averaged conservation equations is described in[8] and only the final results are shown here. By starting with the local single-phase mass and solute mass conservation equation and applying volume-averaging theorems, the averaged mass conservation (Eq. (1)) and the averaged solute conservation equation for species *i* of phase *k* (Eq. (2)) are obtained. The interface balances between phases *k* and *j* are given in Eqs. (3) and (4) for mass and solute mass, respectively. $C_i^{*,k-j}$ is the interface concentration of solute *i* in phase *k* at the *k*-*j* interface, Γ^{k-j} is the mass transfer rate per unit volume from phase *j* to phase *k* due to phase growth, S_v^{k-j} is the specific surface area of the *k*-*j* interface, and δ_i^{k-j} is the diffusion length in phase *k* at the *k*-*j* interface. The volume fraction, density, diffusion coefficient, velocity, and the average solute concentration of phase *k* are given by $g_k, \rho_k, D_k, \langle \vec{v}_k \rangle^k$ and $\langle C_{i,k} \rangle^k$, respectively.

$$\frac{\partial}{\partial t}(\rho_k g_k) + \nabla.\left(\rho_k g_k \langle \vec{v}_k \rangle^k\right) = \sum_{j \neq k} \Gamma^{k-j} \tag{1}$$

$$\frac{\partial}{\partial t}\left(\rho_k g_k \langle C_{i,k} \rangle^k\right) + \nabla.\left(\rho_k g_k \langle \vec{v}_k \rangle^k \langle C_{i,k} \rangle^k\right) = \nabla.\left(\rho_k D_{i,k} g_k \nabla \langle C_{i,k} \rangle^k\right) + \sum_{j \neq k}\left[\Gamma^{k-j} C_i^{*,k-j} + \frac{\rho_k S_v^{k-j} D_{i,k}}{\delta_i^{k-j}}\left(C_i^{*,k-j} - \langle C_{i,k} \rangle^k\right)\right] \tag{2}$$

$$\Gamma^{k-j} + \Gamma^{j-k} = 0 \tag{3}$$

$$\left[\Gamma^{k-j} C_i^{*,k-j} + \frac{\rho_k S_v^{k-j} D_{i,k}}{\delta_i^{k-j}}\left(C_i^{*,k-j} - \langle C_{i,k} \rangle^k\right)\right] + \left[\Gamma^{j-k} C_i^{*,j-k} + \frac{\rho_j S_v^{j-k} D_{i,j}}{\delta_i^{j-k}}\left(C_i^{*,j-k} - \langle C_{i,j} \rangle^j\right)\right] = 0 \tag{4}$$

We neglect the first term on the right hand side of Eq. (2) based on the last assumption mentioned in the previous section.

2.3. Three-phase volume-averaged approach to dendritic equiaxed solidification

For equiaxed dendritic solidification, three phases are modeled: the solid (*s*), intragranular liquid (*d*) and extragranular liquid (*e*). We assume no direct interaction between the solid phase and the extragranular liquid, as expressed in Eq. (5). A simple 1D illustration can be seen in Figure 2. Using of the interface balance in Eq. (3) and introducing the averaged transfer rates of solid mass and of envelope mass Γ^s and Γ^{env}, respectively, the notation of the phase mass transfer rate is reduced to Eq. (6). Similarly, we simplify the notation for the specific surface area, as given by Eq. (7). Furthermore, since the intra- and extragranular phases represent the continuous liquid phase, the interface concentrations at the *e*-*d* interface must be identical, as expressed by Eq. (8). The solid-liquid interface, *s*-*d*, is assumed to be at thermodynamic equilibrium, as expressed by Eq. (9). Also, the densities of the intragranular and extragranular liquid are equal ($\rho_l = \rho_d = \rho_e$).

$$\Gamma^{s-e} = \Gamma^{e-s} = 0, \quad S_v^{s-e} = S_v^{e-s} = 0 \tag{5}$$

$$\Gamma^s = \Gamma^{s-d} = -\Gamma^{d-s}, \quad \Gamma^{env} = \Gamma^{d-e} = -\Gamma^{e-d} \tag{6}$$

$$S_v^s = S_v^{s-d} = S_v^{d-s}, \quad S_v^{env} = S_v^{d-e} = S_v^{e-d} \tag{7}$$

$$C_i^{*,d-e} = C_i^{*,e-d} \tag{8}$$

$$C_i^{*,s} = k_{p,i} C_i^{*,d} \tag{9}$$

Now the complete set of averaged mass and solute balance equations for the three phases, *s*, *d*, and *e*, respectively, is presented from Eq. (10) through (15). Interface solute balances are given in Eqs. (16) and (17) for interfaces *s*-*d* and *e*-*d*, respectively.

$$\frac{\partial}{\partial t}(\rho_s g_s) + \nabla.(\rho_s g_s \langle \vec{v}_s \rangle^s) = \Gamma^s \tag{10}$$

$$\frac{\partial}{\partial t}(\rho_l g_d) + \nabla.\left(\rho_l g_d \langle \vec{v}_l \rangle^d\right) = -\Gamma^s + \Gamma^{env} \tag{11}$$

$$\frac{\partial}{\partial t}(\rho_l g_e) + \nabla.(\rho_l g_e \langle \vec{v}_l \rangle^e) = -\Gamma^{env} \tag{12}$$

$$\frac{\partial}{\partial t}\left(\rho_s g_s \langle C_{i,s} \rangle^s\right) + \nabla.\left(\rho_s g_s \langle \vec{v}_s \rangle^s \langle C_{i,s} \rangle^s\right) = \Gamma^s C_i^{*,s-d} + \frac{\rho_s S_v^s D_{i,s}}{\delta_i^{s-d}}\left(C_i^{*,s-d} - \langle C_{i,s} \rangle^s\right) \tag{13}$$

$$\frac{\partial}{\partial t}\left(\rho_l g_d \langle C_{i,d}\rangle^d\right) + \nabla.\left(\rho_l g_d \langle \vec{v}_l\rangle^d \langle C_{i,d}\rangle^d\right) = -\Gamma^s C_i^{*,d-s} + \Gamma^{env} C_i^{*,d-e} + \frac{\rho_l S_v^s D_{i,l}}{\delta_i^{d-s}}\left(C_i^{*,d-s} - \langle C_{i,d}\rangle^d\right) + \frac{\rho_l S_v^{env} D_{i,l}}{\delta_i^{d-e}}\left(C_i^{*,d-e} - \langle C_{i,d}\rangle^d\right) \quad (14)$$

$$\frac{\partial}{\partial t}\left(\rho_l g_e \langle C_{i,e}\rangle^e\right) + \nabla.\left(\rho_l g_e \langle \vec{v}_l\rangle^e \langle C_{i,e}\rangle^e\right) = -\Gamma^{env} C_i^{*,e-d} + \frac{\rho_l S_v^{env} D_{i,l}}{\delta_i^{e-d}}\left(C_i^{*,e-d} - \langle C_{i,e}\rangle^e\right) \quad (15)$$

$$\Gamma^s\left(C_i^{*,d-s} - C_i^{*,s-d}\right) = \frac{\rho_s S_v^s D_{i,s}}{\delta_i^{s-d}}\left(C_i^{*,s-d} - \langle C_{i,s}\rangle^s\right) + \frac{\rho_l S_v^s D_{i,l}}{\delta_i^{d-s}}\left(C_i^{*,d-s} - \langle C_{i,d}\rangle^d\right) \quad (16)$$

$$0 = \frac{\rho_l S_v^{env} D_{i,l}}{\delta_i^{d-e}}\left(C_i^{*,d-e} - \langle C_{i,d}\rangle^d\right) + \frac{\rho_l S_v^{env} D_{i,l}}{\delta_i^{e-d}}\left(C_i^{*,e-d} - \langle C_{i,e}\rangle^e\right) \quad (17)$$

2.4. A simplified formulation of the three-phase model

In this section we introduce several assumptions that will enable us to simplify the formulation of the model, while retaining its principal physical ingredients. First we introduce the assumption of perfect diffusion in the intragranular liquid, as expressed by Eq. (18).

$$\frac{S_v^s D_{i,l}}{\delta_i^{d-s}} \to \infty, \quad \frac{S_v^{env} D_{i,l}}{\delta_i^{d-e}} \to \infty \quad (18)$$

Because the diffusion time at the scale of the secondary arm spacing is much smaller than the solidification time in typical process conditions, the concentration gradients in the intragranular liquid vanish and the average concentration of the intragranular liquid becomes identical to the interface concentration. This is expressed in (19) and we introduce the sole liquid interface concentration, $C_i^{*,l}$.

$$C_i^{*,l} = C_i^{*,d-s} = C_i^{*,d-e} = C_i^{*,e-d} = \langle C_{i,d}\rangle^d \quad (19)$$

Under this assumption the diffusion length in the intragranular liquid tends to infinity and the expressions for the averaged solute diffusion fluxes in the last two terms on the right-hand side of Eq. (14) become indeterminate. By expressing these indeterminate formulations of the flux via the interface balances of Eqs. (16) and (17), a determinate form of the solute conservation equation for the intragranular liquid is obtained:

$$\frac{\partial}{\partial t}\left(\rho_l g_d C_i^{*,l}\right) + \nabla.\left(\rho_l g_d \langle \vec{v}_l\rangle^d C_i^{*,l}\right) = \Gamma^{env} C_i^{*,l} - \Gamma^s C_i^{*,s-d} - \frac{\rho_s S_v^s D_{i,s}}{\delta_i^{s-d}}\left(C_i^{*,s-d} - \langle C_{i,s}\rangle^s\right) - \frac{\rho_l S_v^{env} D_{i,l}}{\delta_i^{e-d}}\left(C_i^{*,l} - \langle C_{i,e}\rangle^e\right) \quad (20)$$

By expanding the first term on the left hand side of Eq. (20) and applying the mass balance for the intragranular liquid in Eq. (11) we finally arrive at Eq. (21) – a formulation of the balance of the solute flux passing from the solid through the intragranular liquid to the extragranular liquid.

$$\rho_l g_d \frac{D C_i^{*,l}}{Dt} = \Gamma^s\left(C_i^{*,l} - C_i^{*,s-d}\right) - \frac{\rho_s S_v^s D_{i,s}}{\delta_i^{s-d}}\left(C_i^{*,s-d} - \langle C_{i,s}\rangle^s\right) - \frac{\rho_l S_v^{env} D_{i,l}}{\delta_i^{e-d}}\left(C_i^{*,l} - \langle C_{i,e}\rangle^e\right) \quad (21)$$

A key step for the simplification of the model is the assumption of identical velocities of the intra- and extragranular liquid phases ($\langle \vec{v}_d\rangle^d = \langle \vec{v}_e\rangle^e = \langle \vec{v}_l\rangle^l$). This assumption allows us to simplify the model to a three-phase growth kinetics model coupled with two-phase macroscopic transport equations. This treatment is different from previous three-phase models, which proposed various assumptions on the velocity of the intragranular (interdendritic) liquid. Appolaire, Combeau & Lesoult[24], Wu & Ludwig[19], and Wu, Fjeld & Ludwig[25] supposed that the interdendritic liquid moves with the same velocity as the

solid. Wang & Beckermann[16,17] introduced a flow partitioning model based on the intragranular drag model of Wang et al[26]. The flow partitioning model indeed indicates that the intragranular velocity at low and moderate grain volume fractions should be closer to the solid than to the liquid velocity. Yet, simplified treatments are viable; Combeau et al[27] successfully used a two-phase dendritic model with a single liquid phase for the simulation of large industrial ingots. By assuming equal velocities of the intragranular and the extragranular liquid we can conveniently sum the conservation equations for the solute in both liquids, Eqs. (14) and (15), respectively. We obtain a solute conservation equation for the whole liquid, i.e. the extra- and intragranular liquids combined. If we additionally account for the mass balances of Eqs. (11) and (12), the equation can be further simplified and the indeterminate diffusion terms are canceled out. It is convenient to express the solute mass balance for the whole liquid in terms of the averaged liquid concentration, $\langle C_{i,l}\rangle^l$, defined by

$$g_l\langle C_{i,l}\rangle^l = g_d C_i^{*,l} + g_e\langle C_{i,e}\rangle^e. \tag{22}$$

The newly formulated solute conservation equation for the liquid is given in Eq. (23).

$$\frac{\partial}{\partial t}\left(\rho_l g_l\langle C_{i,l}\rangle^l\right) + \nabla.\left(\rho_l g_l\langle \vec{v}_l\rangle^l\langle C_{i,l}\rangle^l\right) = -\Gamma^s C_i^{*,l} + \frac{\rho_l S_v^{env} D_{i,l}}{\delta_i^{e-d}}\frac{g_l}{g_e}\left(C_i^{*,l} - \langle C_{i,l}\rangle^l\right) + \rho_l g_d \frac{DC_i^{*,l}}{Dt} \tag{23}$$

$$\frac{\partial}{\partial t}\left(\rho_s g_s\langle C_{i,s}\rangle^s\right) + \nabla.\left(\rho_s g_s\langle \vec{v}_s\rangle^s\langle C_{i,s}\rangle^s\right) = \Gamma^s C_i^{*,s-d} + \frac{\rho_s S_v^s D_{i,s}}{\delta_i^{s-d}}\left(C_i^{*,s-d} - \langle C_{i,s}\rangle^s\right) \tag{24}$$

$$\Gamma^s\left(1-k_{p,i}\right)C_i^{*,l} = \frac{\rho_s S_v^s D_{i,s}}{\delta_i^{s-d}}\left(k_{p,i}C_i^{*,l} - \langle C_{i,s}\rangle^s\right) + \frac{\rho_l S_v^{env} D_{i,l}}{\delta_i^{e-d}}\frac{g_l}{g_e}\left(C_i^{*,l} - \langle C_{i,l}\rangle^l\right) + \rho_l g_d \frac{DC_i^{*,l}}{Dt} \tag{25}$$

Eqs. (23) and (24) now describe the evolution of the averaged concentration in the liquid and solid phases. The solute conservation equation for the intragranular phase, which would give the respective concentration, $\langle C_{i,d}\rangle^d$, is eliminated and the equilibrium concentration, $C_i^{*,l}$, is determined from thermodynamic relations. Eq. (21) takes the form of a solute flux balance that the mass transfer rates and solute diffusion fluxes must satisfy. This balance is also reformulated in Eq. (25) in terms of the average liquid concentration, $\langle C_{i,l}\rangle^l$, to replace the extragranular concentration, $\langle C_{i,e}\rangle^e$.

Through the process of assuming equal velocities of intragranular and extragranular liquid, and perfect mixing in the intragranular liquid, the three transport equations and two interface balances in Eqs. (13) through (17) have now been reduced to two transport equations and one flux balance in Eqs. (23) through (25). The variables $\langle C_{i,d}\rangle^d$ and $C_i^{*,d-e}$ were eliminated in the process. The term involving the material time derivative of $C_i^{*,l}$ in Eqs. (24) and (25) is the variation of the concentration of intragranular liquid concentration during the growth of the grain. It corresponds to the sum of the total local variation at a fixed Eulerian point (partial derivative of the intragranular concentration) and of the contribution due to convection of the intragranular liquid. Because the model is in an Euler-Euler formulation, only the total local variation of the intragranular liquid concentration is known. It is calculated from thermodynamic equilibrium relations. The contribution of convection is calculated only for the average liquid and is not known separately for the intragranular liquid. This information was lost due to the simplification of the model that eliminated the distinct macroscopic solute transport equation for the intradendritic liquid. Generally, the material derivative $DC_i^{*,l}/Dt$ therefore cannot be evaluated. We therefore propose to neglect this term:

$$\rho_l g_d \frac{DC_i^{*,l}}{Dt} \approx 0 \tag{26}$$

By introducing this approximation, the volume-averaged dendritic model, which conceptually remains a three-phase model, is now formulated as a two-phase model, where the averaged liquid and solid phases are the primary unknowns. Instead of three, only two macroscopic transport equations need to be solved for the solute concentration, and the microscale solute transport is described by a single interface balance. As such, the reformulated three-phase model has a structure similar to a two-phase model and is thus significantly easier to implement as a numerical model. A validation study assessing the validity of the approximation introduced in Eq. (26) is conducted in Section 3.

This model is solved using the splitting method[22]. The scheme for operator splitting is described in full detail in the reference and only the main features of the scheme are described here. Two separate stages are considered in the splitting scheme, where in the first, the *transport* stage, the macroscopic transport terms are integrated globally on the whole domain, while neglecting the growth and nucleation terms. Then, in the second, the *growth* stage, the contributions from the phase interaction terms are integrated locally, initialized from the transport solution. Effectively, the two contributions are summed to obtain the total variation. In a fully implicit timestepping formulation this integration scheme is iterated at each timestep.

2.5. Closing relations for the dendritic growth model

Closing relations for the dendritic growth model are given in Table 1. The specific surface area of the solid phase is approximated by that of an equivalent sphere of radius $R^{s,eq}$, based on the volume of solid. The grain envelope is assumed spherical and the growth of the envelope is calculated from the velocity of the primary dendrite tips. The envelope shape can have a noticeable influence on the model predictions[25,28]. Nielsen et al[28] have shown that spherical envelopes tend to result in lower predicted internal solid fractions in the dendritic grains than octahedral envelopes. The proposed model can however easily accommodate other envelope shapes. The dendrite tips are assumed to be hemispherical and the expression for the dependence of the tip velocity, V_{tip}, on the supersaturation of the liquid is taken from Ref.[29] for multi-component alloys. The average diffusion length for the solid phase, δ_i^{s-d}, is taken from Ref.[22] and is calculated for the equivalent solid sphere of radius, $R^{s,eq}$. For the extragranular liquid phase the average diffusion length at the grain envelope, δ_i^{e-d}, is calculated by the stagnant-film model described in Ref.[30]. This model gives the diffusion length for solute transfer from a spherical envelope growing in confined space (due to the presence of other grains) under the influence of convection. The influence of the interface motion is accounted for and the influence of convection is described by a stagnant-film formulation. The corresponding relations for dimensionless supersaturation (Ω), Reynolds number (Re), Sherwood number (Sh), and Schmidt number (Sc) are also presented. The temperature and equilibrium interface composition are linked by a simplified multicomponent phase diagram. The liquidus temperature, T_{liq}, is linearly dependent on the alloy concentration, and the liquidus slopes, $m_{l,i}$, and partition coefficients, $k_{p,i}$, for each species, i, are assumed to be constant.

Table 1: Closing relations for the dendritic growth model

Geometrical relations for the dendritic grains

$$R_f = \left(\frac{3}{4\pi N_g}\right)^{1/3}, \qquad R^{env} = R_f g_{env}^{1/3}, \qquad R^{s,eq} = R_f g_s^{1/3},$$

$$S_v^{env} = 4\pi (R^{env})^2 N_g, \qquad S_v^s = 4\pi (R^{s,eq})^2 N_g$$

Dendrite tip kinetics

$$\Gamma^{env} = \rho_l S_v^{env} V_{tip}$$

$$V_{tip} = \frac{\partial R^{env}}{\partial t} = \left[\frac{\left(D_{i=1}^l\right)^2}{\Gamma_{GT}} \sum_i \frac{m_{l,i} C_i^{*,l} (k_{p,i} - 1)}{D_i^l}\right] (\Omega_{i=1})^2, \qquad \Omega_{i=1} = \frac{g_l}{g_e} \frac{\left(C_{i=1}^{*,l} - \langle C_{i=1,l}\rangle^l\right)}{C_{i=1}^{*,l}(1 - k_{p,i=1})}$$

Diffusion lengths

$$\delta_i^{s-d} = \frac{R^{s,eq}}{5}, \quad \delta_i^{e-d} = d_i \left\{\frac{d_i}{R^{env}} - \frac{f(R^{env},\Delta_i) + g(R_f,R^{env},\Delta_i)}{d_i\left[R^{env}{}_{+d_i} - (R^{env}+\Delta_i+d_i)e^{-\Delta_i/d_i}\right] - f(R^{env},\Delta_i) + (e^{-\Delta_i/d_i}-1)g(R_f,R^{env},\Delta_i)}\right\}^{-1}$$

$$d_i = D_{l,i}/V_{tip}, \qquad f(R_{env},\Delta_i) = \frac{\left[(R^{env}+\Delta_i)^2 - (R^{env})^2\right]}{2}, \qquad g\left(R_f,R^{env},\Delta_i\right) = \frac{\left[\left(R_f\right)^3 - (R^{env}+\Delta_i)^3\right]}{[3(R^{env}+\Delta_i)]}$$

$$\Delta_i = \frac{2R^{env}}{Sh_i}, \qquad Sh_i = \frac{2}{3(1-g_{env})} Sc_i^{\frac{1}{3}} Re^{n(Re)}, \qquad Sc_i = \frac{\mu_l}{\rho_l D_{l,i}}, n(Re) = \frac{2Re^{0.28}+4.65}{3(Re^{0.28}+4.65)}$$

$$Re = \frac{\rho_l (1-g_{env})(2R^{env})}{\mu_l} \left|\langle \vec{v}_s\rangle^s - \langle \vec{v}_l\rangle^l\right|$$

Phase diagram

$$C_i^{*,s-d} = k_{p,i} C_i^{*,l}, \quad T_{liq} = T_m + \sum_i m_{l,i} c_{l,i}^*$$

2.6. Modeling of nucleation

Nucleation of grains in aluminum alloys is assumed to occur on grain-refiner (inoculant) particles. According to the athermal nucleation theory of Greer et al.[31], the critical undercooling for free growth of a grain on an inoculant particle of diameter d is given by $\Delta T_c(d)=4\Gamma_{GT}/d$, where Γ_{GT} is the Gibbs-Thompson coefficient. According to this model the activation of an inoculant particle is instantaneous as soon as the constitutional undercooling of the liquid becomes large enough. The undercooling is given by Eq. (27). The number of activated particles then depends on the size distribution of the particle population, which can be represented by an exponential distribution density function given by Eq. (28).

$$\Delta T = \sum_i m_{l,i}\left(C_i^{*,l} - \langle C_{i,e}\rangle^e\right) \tag{27}$$

$$n(d) = \frac{N_0}{d_0} exp\left(-\frac{d}{d_0}\right) \tag{28}$$

N_0 is a characteristic inoculant population density and d_0 is the characteristic width of the distribution. This representation holds for the largest particles, which are activated at small undercoolings and therefore successful as nuclei. The full distribution, including the smaller particles, can be described by a Gaussian[31,32] or a log-normal distribution[33]. In our modeling, the size distribution is first transformed into a distribution with respect to the activation undercooling, ΔT_c. This gives the following distribution density function.

$$n(\Delta T_c) = \frac{4\Gamma_{GT} N_0}{\Delta T_c^2 d_0} exp\left(-\frac{4\Gamma_{GT}}{d_0 \Delta T_c}\right) \tag{29}$$

This distribution is then discretized into m classes of inoculants. Each class, i, is represented by a volumetric population density, N^i_{nuc}, and a critical undercooling, ΔT_c^i. They are determined by taking the portion of the distribution in Eq. (29) that covers the range between the smallest and the largest inoculant particles measured experimentally and dividing it into m intervals with respect to the undercooling, ΔT_c. N^i_{nuc} is then the integral of the distribution density function (Eq. (29)) over the i-th interval. ΔT_c^i is the arithmetic mean of the two undercoolings delimiting the i-th interval. When the local undercooling reaches the critical undercooling of class i, its local inoculant density, N^i_{nuc}, is instantaneously added to the grain density, N_G, and N^i_{nuc} becomes locally zero. The population balances for the density of each inoculant class and for the grain density are Eqs. (30) and (31), respectively, where Φ^i represents the transfer of population density from inoculants of class i to grains upon nucleation and δ is the Dirac delta function.

$$\frac{\partial}{\partial t}\left(N^i_{nuc}\right) + \nabla.\left(\langle\vec{v}_l\rangle^l N^i_{nuc}\right) = -\Phi^i \tag{30}$$

$$\Phi^i = \begin{cases} N^i_{nuc}\,\delta(t-t_o)\ , & \Delta T(t_0) < \Delta T_c^i \\ 0\ , & \text{else} \end{cases} \quad , i = 1, \dots, m$$

$$\frac{\partial}{\partial t}\left(N_g\right) + \nabla.\left(\langle\vec{v}_s\rangle^s N_g\right) = \sum_{i=1}^{N^i_{nuc}} \Phi^i \tag{31}$$

2.7. Conservation of energy

As local thermal equilibrium is assumed, the enthalpy of the intra- and extragranular liquid is identical and equal to the averaged liquid phase. The definition of the volume-averaged mixture enthalpy and the energy conservation equation follow from Ref.[22] and are given by Eqs. (32) and (33), respectively.

$$\langle h_s\rangle^s = c_p T, \qquad \langle h_l\rangle^l = c_p T + L_f, \qquad h_m = \rho_s g_s \langle h_s\rangle^s + \rho_l g_l \langle h_l\rangle^l \tag{32}$$

$$\frac{\partial}{\partial t}(\rho_m h_m) + \nabla.(\rho_s g_s \langle\vec{v}_s\rangle^s \langle h_s\rangle^s) + \nabla.\left(\rho_l g_l \langle\vec{v}_l\rangle^l \langle h_l\rangle^l\right) = \nabla.((g_l k_l + g_s k_s)\nabla T) \tag{33}$$

2.8. Conservation of momentum

As the intrinsic velocities of the intra- and extragranular liquid are assumed equal, the momentum equations are derived for the averaged liquid and solid phase. The grains move freely everywhere where the envelope fraction, g_{env}, is smaller than the imposed volume fraction for grain packing, g_{pack}. When the envelope fraction exceeds the packing fraction, the grains are assumed to form a rigid porous solid matrix moving with the casting velocity, $\vec{V}_{cast}$. For the moving solid phase, the inertial and viscous terms are neglected in the momentum balance. Furthermore, the inter-phase momentum transfer due to nucleation and growth is assumed to be negligible. Following the derivation in Ref.[22], the liquid and solid momentum equations are given in Eqs. (34) and (35), respectively. The interfacial drag term, given in Eq. (37), is modeled in the same manner as in Ref.[34] for spherical particles, with the exception that the particle size is now evaluated based on the envelope volume and radius (g_{env}, R^{env}) rather than the solid volume and equivalent radius (g_s, $R^{s,eq}$). As a result, for a given solid fraction the drag force increases as the grain becomes more dendritic. When the envelope volume fraction exceeds the packing fraction, g_{pack}, and the solid phase forms a porous rigid structure, the interfacial drag is modeled by a Darcy term. The hydrodynamic permeability, K, is calculated from the Kozeny-Carman relation, using a characteristic length of the porous structure, l_{KC}.

$$\frac{\partial}{\partial t}\left(\rho_l g_l \langle\vec{v}_l\rangle^l\right) + \nabla.\left(\rho_l g_l \langle\vec{v}_l\rangle^l \langle\vec{v}_l\rangle^l\right) = -g_l \nabla p_l + \nabla.\left(g_l \mu_l \nabla \langle\vec{v}_l\rangle^l\right) + g_l \rho_l^b \vec{g} + M_{ls} \tag{34}$$

$$\begin{cases} 0 = -g_s \nabla p_l + g_s \rho_s^b \vec{g} - M_{ls} & g_{env} < g_{pack} \\ \langle\vec{v}_s\rangle^s = \vec{V}_{cast} & g_{env} > g_{pack} \end{cases} \tag{35}$$

$$\rho_l^b = \rho_o \left(1 - \beta_T\left(T - T_{ref}\right) - \sum_i \beta_{C,i}\left(\langle C_{i,l}\rangle^l - C_{ref}\right)\right) \tag{36}$$

$$M_{ls} = \begin{cases} \frac{3 g_{env} C_D \mu_l Re}{4(2R_{env})^2 (1 - g_{env})}\left(\langle\vec{v}_s\rangle^s - \langle\vec{v}_l\rangle^l\right) & g_{env} < g_{pack} \\ \frac{g_l^2 \mu_l}{K}\left(\langle\vec{v}_s\rangle^s - \langle\vec{v}_l\rangle^l\right), K = \frac{{l_{KC}}^2}{180}\frac{{g_l}^3}{\left(1 - g_l\right)^2} & g_{env} > g_{pack} \end{cases} \tag{37}$$

3. Validation of the approximate dendritic model

The approximation introduced in Eq. (26) could significantly affect the predictions of the model. The approximate model must therefore be tested by comparison to the full three-phase model. The comparison will enable us to estimate the error made by neglecting the accumulation of solute in the intragranular liquid. The test configuration is a small, initially liquid sample of a binary alloy, solidified by cooling with a constant heat flux. This corresponds to a closed isothermal system, without mass and solute exchange with the environment (which is equivalent to setting all velocities in the conservation equations to zero: $\langle\vec{v}_s\rangle^s = \langle\vec{v}_l\rangle^l = 0$). A constant volumetric heat sink ($\dot{q}$) extracts the heat necessary to solidify the binary alloy. In this situation, there is no fluid and no solid motion, thus all convective terms are nil. The substantial derivative of the intragranular concentration is then simply equal to the total time derivative, $\frac{DC_i^{*,l}}{Dt} = \frac{\partial C_i^{*,l}}{\partial t}$. This means that the accumulation term that is neglected in the approximate model can be easily calculated and the full three-phase model is thus recovered. Consequently, the complete dendritic model can be resolved and the error arising from the approximate model can be assessed. Both the full and the approximate three-phase models are additionally compared to the three-phase model of Wang and Beckermann[18].

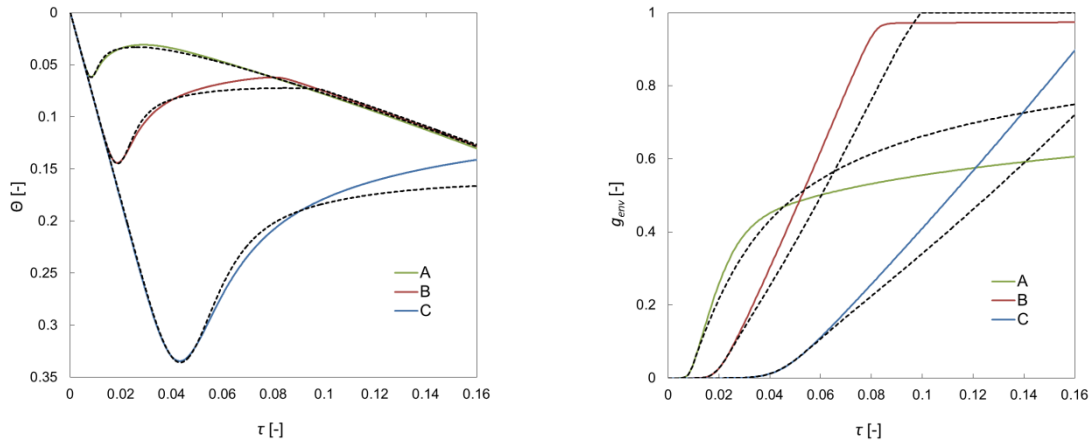

a) b)

Figure 3: Evolution of a) the dimensionless temperature and b) envelope volume fraction as a function of dimensionless time shown for the proposed complete dendritic model (solid lines) and approximate dendritic model (dashed lines). The three cases are defined as A: N_g=2.39x10^{11} m^3, B: N_g=2.39x10^8 m^3, C: N_g=2.39x10^5 m^3. The dimensionless temperature is given by $\theta = \frac{T_o - T}{T_o - T_{eut}}$, and the dimensionless time is given by $\tau = (\frac{\dot{q}}{L_f})t$.

The test case is that of solidification of a binary Al-5wt.%Si alloy, described in Ref.[18,13]. Three densities of the grain population, N_g, are considered, leading to different levels of solutal interaction between the grains and thus to different levels of growth kinetics. All thermophysical properties are defined in Ref.[13]. The diffusion in the solid is assumed to be nil in this test case. The evolution of the dimensionless temperature, $\theta = (T_0 - T)/(T_0 - T_{\text{eut}})$, and of the envelope volume fraction as a function of dimensionless time, $\tau = (\frac{\dot{q}}{L_f})t$, are shown in Figure 3 for the complete and the approximate model for the three cases. The complete dendritic model perfectly matches the results of Wang and Beckermann[18]; the comparison is not shown in Figure 3 because the curves superpose entirely. In all three cases the nucleation is triggered at the liquidus temperature $\theta = 0$ at $\tau = 0$. The temperature then drops quickly down to a minimum and then undergoes recalescence. This stage indicates a strong departure of the extradendritic liquid from equilibrium (constitutional undercooling). As growth progresses, interaction between grains starts due to soft impingement and the concentration of the extradendritic liquid starts to approach equilibrium. Equilibrium is indicated by the baseline of the temperature curve in the plot in Figure 3a. Interactions start later for smaller grain densities and the maximum departure from equilibrium (undercooling) is thus larger. A substantial decrease of the envelope growth rate is noticed when the liquid approaches equilibrium (Fig. 3b). Although the tip growth speed is much larger at higher undercoolings, the time needed for the envelopes to fill the space is longer at lower grain densities. Note that the mean distance between grains varies as $d_f \propto N_v^{-1/3}$.

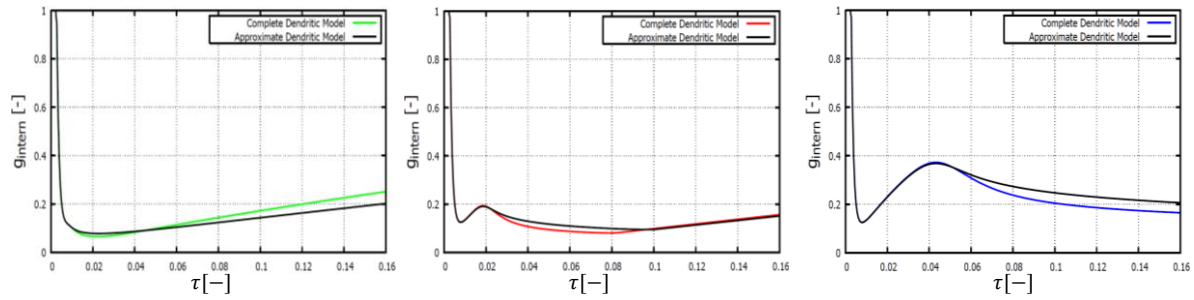

a) b) c)

Figure 4: Evolution of the internal solid fraction, g_{intern}, for a) N_g=2.39x10^{11} m^3, b) N_g=2.39x10^8 m^3 and c) N_g=2.39x10^5 m^3, for the proposed complete dendritic model (colored line) and approximate dendritic model (black line). The dimensionless time is defined as: $\tau = (\frac{\dot{q}}{L_f})t$.

The approximate model predicts the same temperature evolution as the complete model up to the lowest recalescence temperature. The two models start to differ during the temperature increase. Initially the approximate model displays a steeper temperature increase after recalescence. Consequently, the undercooling is smaller compared to the complete model and the envelopes therefore grow at a slower rate. During later stages of recalescence the approximate model gives a higher undercooling than the complete model and the envelopes thus keep growing, while the envelope growth slows down for the complete model because of the smaller predicted undercooling. As a result, the approximate model gives a less dendritic morphology during the early stages of recalescence, while the final grain morphology is more dendritic than that predicted by the complete model, especially for Case A, as shown in Figure 4(a-c). Morphology description here is given by measuring the internal solid fraction ($g_{intern} = g_s/g_{env}$). The grain is globular as g_{intern} approaches one and is dendritic as $g_{intern} \ll 1$. In order to analyze the role of the different solute fluxes in the predicted growth kinetics, Figure 5 shows the evolution of the individual terms in the solute flux balance of Eq. (25) as a function of dimensionless time. Note that the case is defined with zero solid diffusion, thus only three terms are shown. The variation of the intragranular liquid concentration depends linearly on the temperature variation and can thus be directly related to the cooling curves shown in Figure 3a. During the initial sharp temperature decrease the fraction of the intragranular liquid is very small and therefore the neglected term of the approximate model, $g_d \frac{\partial c_i^{*,l}}{\partial t}$, is negligible. During recalescence the neglected term represents around 20% of the contribution of the remaining terms, which can be seen in Figure 5a, Figure 5b, and Figure 5c. By neglecting the term, the solidification rate is increased (Γ^s), and the release of latent heat decreases the undercooling, as noted in the previous paragraph. It should be noted that when the constitutional undercooling of the extragranular liquid becomes small, this neglected term becomes important, as can be seen from Figure 5b. The reason is that when the envelopes coalesce (at $\tau \approx 0.09$, in Case B) the only liquid remaining is the intragranular liquid. All solute rejected by the growing solid is thus rejected into the intragranular liquid.

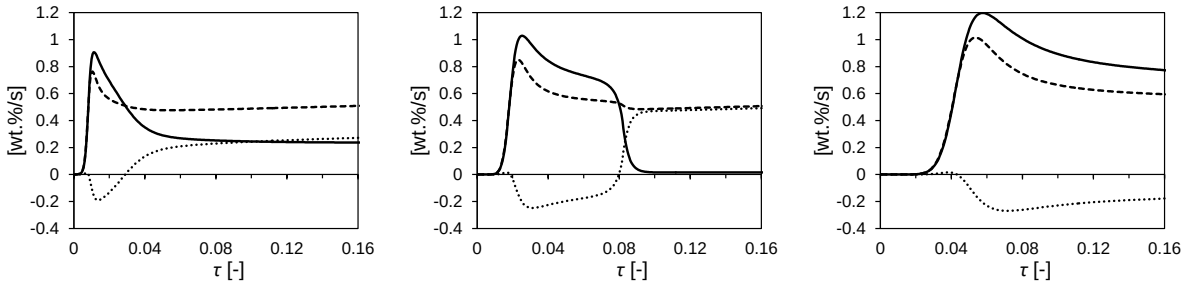

a) b) c)

Figure 5: Evolution of the different terms in Eq. (25) for a) N_g=2.39x10^{11} m^3, b) N_g=2.39x10^8 m^3 and c) N_g=2.39x10^5 m^3, calculated with the complete dendritic model. The different terms are shown as:

$$\cdots\cdots g_d \frac{DC_i^{*,l}}{Dt}, \qquad \text{-----} \frac{\Gamma^s}{\rho_l}(1-k_{p,i})C_i^{*,l}, \qquad \text{——} \frac{S_v^{env} D_{i,l}}{\delta_i^{e-d}} \frac{g_l}{g_e}\left(C_i^{*,l} - \langle C_{i,l}\rangle^l\right)$$

The cases shown in Figure 3 and Figure 5 test the approximate model for a wide range of grain interaction levels due to the varying distance between grains. The neglected term is generally expected to be larger at fast temperature variations and strongly dendritic grain morphologies (large intragranular liquid fraction). This corresponds to Case C, which has a high cooling rate and a small grain density. In order to assess the error in a more general manner and for a wider range of process and material parameters, the case by Wang and Beckermann[18] is additionally calculated for three different nominal solute concentrations of the alloy, C_o, and over a larger range of grain sizes. In a more general framework, the influence of C_o shows the influence of the growth restriction factor, $Q_{si} = C_{o,Si} m_{l.Si}(k_{p,Si} - 1)$, a characteristic temperature range of solidification. The influence of the grain size can be generalized to the influence of the Fourier number in the liquid. The Fourier number is the ratio between the solidification time t_{sol} and the diffusion time in the liquid at the grain scale, and thus characterizes the grain growth kinetics. It is defined as $Fo = D_{Si,l} t_{sol}/R_f^2$, where R_f is the final grain radius. The error of the approximate model is assessed in terms of the maximum undercooling occurring during solidification and of the morphology factor, defined in Eq. (38).

$$f_{morphology} = \left(\frac{1}{g_{env}|_{g_s=0.5}} - 1\right) \tag{38}$$

By recording the value of the envelope fraction at the instant when the solid fraction reaches 0.5, $g_{env}|_{g_s=0.5}$, a measure of morphology can be formulated. The factor ranges from 1.0 for globular morphology ($g_{env}|_{g_s=0.5}$) to 0.0 for dendritic morphology ($g_{env}|_{g_s=0.5} = 1.0$). The maximum undercooling is an essential output of the growth model for coupling with nucleation. The predicted maximum undercooling and morphology factor are shown in Figure 6 for the complete and approximate models. It is observed that the maximum undercooling is generally predicted very accurately by the approximate model and the relative error remains between 0.0% to +0.5 % for all data points. This is in accordance with the recalescence curves shown in Figure 3a, where the error at maximum undercooling was already shown to be small. Figure 6b shows that the transition from globular to dendritic morphology occurs in the range of Fourier numbers between 0.01 to 10 for the complete model. On the other hand, the approximate model displays a narrower transition range and fully dendritic morphology occurs at a Fourier numbers that are an order of magnitude higher than in the complete model. Thus, the approximations made in the solute conservation equations result in the prediction of a more globular microstructure compared to the complete model.

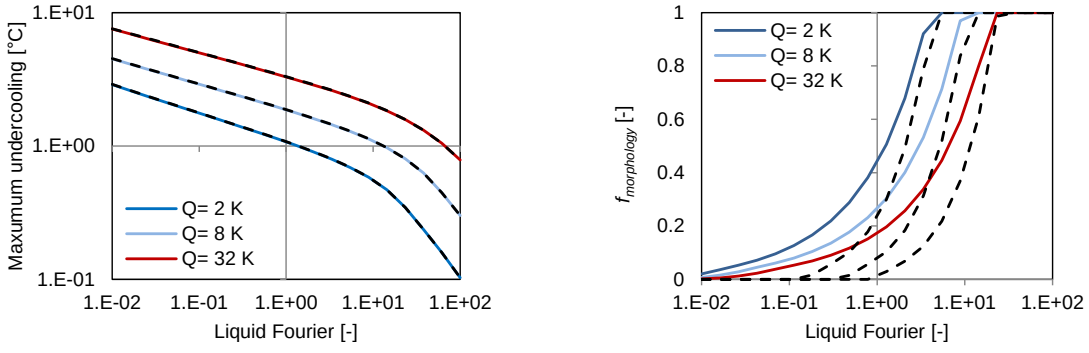

Figure 6: Predicted a) maximum undercooling and b) grain morphology shown for complete dendritic model (solid lines) and approximate model (dashed lines) for three different growth restriction factors ($Q_{si} = C_{o,Si} m_{l.Si}(k_{p,Si} - 1)$) as a function of the liquid Fourier number ($Fo = D_{Si,l} t_{sol}/R_f^2$).

4. Application of the model to DC casting

4.1. Case description

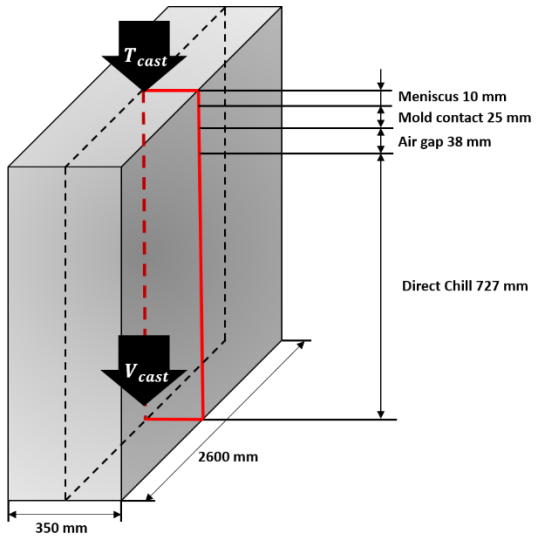

Figure 7: Ingot geometry with corresponding boundary conditions given in Table 2**.**

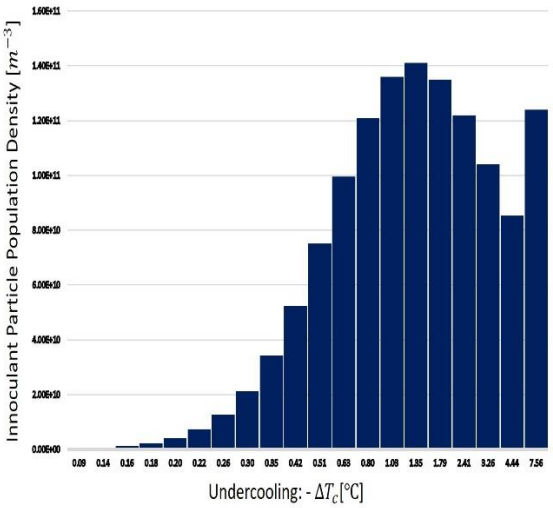

Figure 8: Distribution of the inoculant particle population density with respect to the activation undercooling. 20 particle classes were used.

As a first application of the simplified three-phase dendritic model on a casting process we simulate an industrial scale aluminum-alloy DC casting and we study the impact of the equiaxed grain morphology on macrosegregation. The DC casting geometry and the alloy system used are based on the case study performed by Založnik et al.[23] with slightly different boundary conditions. An industrial scale ingot with thickness of 350 mm is considered. The geometry is simplified to 2D and symmetry is assumed at the central axis. The schematics of the simulation domain is shown in Figure 7. Liquid metal maintained at the casting temperature, T_{cast}, the reference solute concentration, C_o, and the nominal inoculant population density, N^i_{nuc}, enters the domain through the mold inlet at the top. The inlet velocity is calculated based on a mass balance accounting for solidification shrinkage. The solidified metal leaves the domain at the bottom at a predefined casting speed, V_{cast}, of 60 mm/min. The acceleration due to gravity, g = –9.81 m/s^2 is in the vertical direction. The heat is extracted by primary cooling through the mold by and by secondary cooling directly to the falling water film flowing over the ingot surface. Primary cooling consists of three zones: meniscus, mold, and air gap. The boundary conditions are specified in Table 2. The heat transfer coefficient due to secondary cooling is modeled using the Weckmann-Niessen[35] correlation,

$$h_{secondary}(T) = \{A + B \cdot (T[\mathrm{K}] + T_{water}[\mathrm{K}])\} \cdot \left(\frac{Q_{water}}{P}\right)^{\frac{1}{3}} + C \cdot \frac{(T - T_{sat})^3}{T - T_{water}} \tag{39}$$

$$A = -167000\ [\mathrm{W{\cdot}s^{\frac{1}{3}}{\cdot}m^{-8/3}}]; \qquad B = 352\ [\mathrm{W{\cdot}s^{1/3}{\cdot}m^{-8/3}{\cdot}K^{-1}}]; \qquad C = 20.8\ [\mathrm{W{\cdot}m^{-2}{\cdot}K^{-2}}]$$

Where $h_{\mathrm{Secondary}}$ is the heat transfer coefficient, T is the surface temperature of the ingot, T_{water} is the water temperature, T_{sat} is the boiling temperature of the water, Q_{water} is the water volumetric flow rate per ingot, and P is the ingot perimeter. All parameter values are given in Table 2.

Table 2: Boundary Conditions for Energy, Liquid Momentum and Solid Momentum

Boundary	Energy	Liquid Momentum	Solid Momentum
Inlet	T_{cast} = 953.15 K	calculated	-
Meniscus	h = 1 W/(m^{2}K) , T_{amb} = 293.15 K	Nonslip	Nonslip
Mold Contact	h = 350 W/(m^{2}K) , T_{amb} = 293.15 K	Nonslip	Nonslip
Air Gap	h = 50 W/(m^{2}K) , T_{amb} = 293.15 K	Nonslip	Nonslip
Direct Chill	Based on Equation (39) T_{water} = 293.15 K, T_{sat} = 373.15 K $Q_{water} = 20\ l/min$	Nonslip	Nonslip
Outlet	-	-	V_{cast}

The size distribution of TiB_2 inoculant particles taken from Ref.[32] for 2 kg/ton of Al-Ti-B grain refiner is shown in Figure 8. The distribution of inoculant particle population density against the undercooling is plotted. In this study, the inoculant distribution is discretized into 20 classes (m=20). It should be noted that the grain refiner type and particle distribution density used here are different from the one used in Založnik et al[23], where 0.4 kg/ton of Al-Ti-C grain refiner was used.

The 7449 alloy system was modeled as an equivalent pseudo-binary Al-Zn alloy[23]. The linearized phase diagram of the binary alloy, defined by the liquidus slope, the partition coefficient, and the melting temperature of pure Al, has been adjusted to fit the solidification path of AA7449, calculated from a CALPHAD model[23]. The upper limit of the envelope fraction for moving grains, called packing fraction, is set to 0.3. The thermophysical properties of the pseudo-binary alloy are given in Table 3. For the mass balances the densities of solid and liquid phase are different, but are assumed to be constant.

The transport equations were solved with a finite volume method and the SIMPLE algorithm for staggered grid was used for pressure-velocity coupling. The convective terms were discretized with a first-order upwind scheme and for time discretization a fully implicit first-order scheme was used. For all simulations, a structured grid of 16384 cells ($N_x \times N_y$=64×256) was employed. A constant time step of 0.02 s was used and the calculations were run until steady state.

Table 3: Thermophysical data for Al-Zn binary alloy used in the numerical simulations.

Property	Unit	Value	Property	Unit	Value
c_p	J.kg^{-1}K^{-1}	1.3x10^3	ρ_l	kg/m^3	2519.0
L_f	J kg^{-1}	3.63x10^5	ρ_s	kg/m^3	2662.5
Γ_{GT}	K.m	1.9x10^{-7}	ρ_s^b	kg/m^3	2662.5
μ_l	N.S.m^{-2}	1.28x10^{-3}	ρ_{l0}	kg/m^3	2519.0
k_l	W.m^{-1}K^{-1}	75.0	β_T	K^{-1}	1.5 x10^{-4}
k_s	W.m^{-1}K^{-1}	185.0	l_{KC}	m	1.0 x10^{-4}
T_m	K	950.95	g_{pack}	-	0.3
T_{eut}	K	750.70	D_l	m^2 s^{-1}	5.66 x10^{-9}
C_0	wt.%	8.375	D_s	m^2 s^{-1}	5.60 x10^{-13}
k_p	-	0.257	β_c	(wt.%)$^{-1}$	-1.23 x10^{-2}
m_l	Kwt.%$^{-1}$	-6.05			

4.2. Results and Discussion

We investigate the impact of grain morphology on macrosegregation in the DC cast ingot. This study extends the investigation of Založnik et al.[23,36] on the influence of the motion of globular grains on macrosegregation. For a given alloy and for given solidification conditions the grain morphology depends principally on the final grain size, which is given by the number of nucleated grains per unit volume. At high grain densities the grains become globular due to the strong solutal interactions between growing grains; at lower grain densities the grains develop a dendritic morphology[37]. We can thus control the grain morphology by varying the inoculant particle population density. The reference inoculant particle density distribution, given in Figure 8, is for 2 kg/t of Al-5Ti-1B grain refiner. This corresponds to two cases – Case 2a and Case 2b. In Case 2a, globular grain growth is assumed by imposing $g_{env} = g_s$. By doing this, the grain envelope is assumed to be same as the solid volume, resulting in the internal solid fraction of 1. This imposes a globular grain morphology. In Case 2b, the grain morphology is simulated, revealing the impact of dendritic grain growth. The same comparison is made with a reduced inoculant density by ten times (Cases 1a and 1b) and with an increased inoculant density by ten times (Cases 3a and 3b). This is achieved by multiplying or dividing N_0 in Eq. (29) by 10; the shape of the distribution of the activation undercooling of the inoculant particles thus stays the same. A summary of the cases can be seen in Table 4.

Table 4: Simulation Cases

Driving Mechanisms	**Growth Model**		**Description**
	Globular	**Dendritic**	
SH+NC+GM	Case 1a	Case 1b	0.2 kg/t
SH+NC+GM	Case 2a	Case 2b	2 kg/t (Reference)
SH+NC+GM	Case 3a	Case 3b	20 kg/t

Figure 10 shows the macrosegregation in all six cases. Figure 11 (a-c) shows the comparison of the relative segregation across the ingot cross-section, predicted by the globular and dendritic growth models for different grain refiner levels. Figure 11d depicts the horizontal profile of internal solid fraction (g_{intern}) for Cases 1b, 2b and 3b.

A dendritic grain is represented by a solid skeleton (g_s) that is circumscribed by a grain envelope (g_{env})[38]. The volume of the envelope depends on the growth velocity of the primary dendrite tip, whereas the volume of the solid skeleton depends on the rate of solidification or melting given by the mean velocity of the solid-liquid interface. Thus, the evolution of dendritic grain morphology can be understood as a result of competition between the dendrite tip velocity and the mean interface velocity. The tip growth is promoted with increase in undercooling[38] and undercooling is linked again to grain density[24]. For a given cooling configuration, a higher grain density increases the total grain surfaces rejecting solute into the surrounding intergranular liquid. The concentration gradient around the grain decreases, resulting in lower undercooling. This decrease in undercooling slows down or effectively blocks dendritic tip growth. With increase in grain density, the morphology therefore tends to be more globular. For decreasing grain density, the grain tends to be more dendritic. A measure of morphology can be obtained by the ratio between the volume of the solid phase and the volume of the envelope, the internal solid fraction: $g_{intern} = g_s/g_{env}$. The grain is globular as g_{intern} approaches one and is dendritic as $g_{intern} \ll 1$. The grain morphology also affects the grain motion. For dendritic grains it is more reasonable to consider that they pack at a certain envelope fraction, g_{env}, rather than a solid fraction, g_s. Dendritic grains therefore effectively pack at lower solid fractions than globular grains ($g_{env} \gg g_s$).

The velocity field for the solid phase $\langle \vec{v}_s \rangle^s - \vec{V}_{cast}$ and the development of the dendritic grain morphology by measuring g_{intern} in the mushy zone of the casting are shown in Figure 9 (a-c) for Cases 1b, 2b and 3b. Note that a virtually steady state is obtained and the solid velocity vectors thus indicate the grain trajectories. Due to an intricate coupling between the grain nucleation, growth, heat transfer, and flow, all grains nucleate in an elongated narrow region in the outer zones of the casting[23,39]. The initial grain morphology upon nucleation is assumed to be globular, before the dendritic ramifications develop. The nucleation region is thus clearly visible as a narrow zone of globular grains. On their way through the mushy zone the grains then develop a dendritic morphology. The extent of the dendritization depends on the grain density, as discussed before. At lower nucleation densities the grains are clearly more dendritic. This can be seen in Figure 9a. It corresponds to a case with low grain density and the grains are packed at very low internal solid fraction, indicating dendritic morphology. As we move to higher grain densities, from Figure 9b to Figure 9c, grains pack at higher internal solid fraction values, indicating globularization. Furthermore, the morphology evolution of the grains depends on their trajectory through the mushy zone. A part of the grains travels through the central part of the slurry zone before settling to the bottom or rejoining the main current of descending grains. Because the central zone has a very low undercooling the growth conditions there promote globularization. The final grain morphology at the packing front therefore depends not only on the number of nucleated grains, but also on the macroscopic flow pattern that determines the trajectory of the grains through zones with different solidification conditions.

The grain morphology has a decisive impact on macrosegregation, an important defect of chemical homogeneity in DC casting. The origin of macrosegregation in DC casting is attributed to three different phenomena of solute transport: motion and packing of equiaxed grains, melt flow due to thermosolutal natural convection and due to entrainment by the solid grains, and melt flow induced by solidification shrinkage[23]. Grain motion carries settling solute-lean solid grains towards the center of the ingot and thus causes negative segregation at the center with immediate positive segregation in the mid-section. Natural convection causes negative segregation close to the surface and reduces the grain settling velocity in the center, in turn reducing the negative segregation at the center. Shrinkage induced flow has an important contribution to macrosegregation only at high solid fraction and thus acts entirely in the region of packed grains. It promotes negative segregation at the center and slightly positive segregation in the other parts of the domain.

With varying grain refiner, the macrosegregation intensity changes, even though the fundamental way in which transport mechanisms act remains unchanged. Let us consider Cases 1a, 2a and 3a, corresponding to the globular grain growth model. In this case, the internal solid fraction is 1, as we impose $g_s = g_{env}$. Referring to Table 1, the grain radius ($R^{s,eq}$) is inversely related to grain density (N_g). As grain density is reduced, the grain size increases, which results in an increase in relative velocity between solid and liquid. This manifests itself by increased negative segregation at the center, resulting in large regions of enriched zone above the slurry region, as seen in Figure 10a. While the shape of the macrosegregation profile remains similar, the negative segregation in the center and the corresponding enriched zone above the slurry region reduce as we move from Case 1a (Figure 10a) to Case 2a (Figure 10c) and to Case 3a (Figure 10e). This sequence corresponds to an increasing grain refiner level resulting in a decreasing size of globular grains, which in turn leads to less negative segregation at the center. The average grain size for all cases is summarized in Table 5.

Table 5: Average equivalent Grain Diameter (μm)

Case 1a	Case 1b	Case 2a	Case 2b	Case 3a	Case 3b
253	360	133	191	80	96

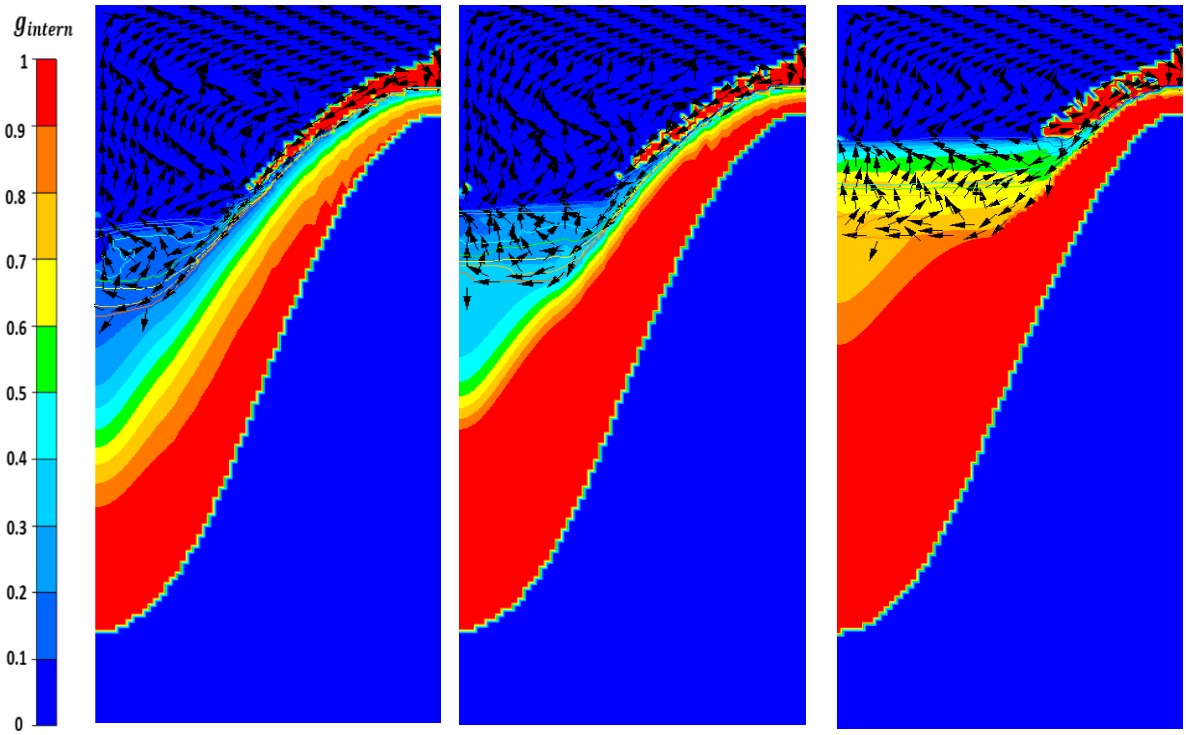

Figure 9: Internal solid fraction g_{intern} fields with envelope fraction g_{env} isolines from 0 to g_{pack} for a) Case 1b, b) Case 2b and c) Case 3b. Relative solid velocity vectors $\langle \vec{v}_s \rangle^s - \vec{V}_{cast}$ are plotted.

Unlike for globular grains, the solid mass transported due to settling of dendritic grains is quite small and the impact of the transport of the solid phase on the macrosegregation is reduced. Furthermore, a packed layer of dendritic grains is looser (has a higher liquid fraction) and can therefore have a higher permeability than a packed layer of globular grains. This promotes the percolation of intragranular liquid due to natural convection through the packed zone. As a result, positive segregation in the center and negative segregation close to the surface are observed. This can be seen in Figure 10b. The influence of the grain morphology on macrosegregation is clearly seen by comparing simulations with dendritic growth in the order of increasing grain refiner addition: Cases 1b, 2b, and 3b (Figure 10b, Figure 10d, and Figure 10f, respectively). As the grain refiner addition level increases, the shape of the macrosegregation profile changes significantly. The centerline segregation moves from strongly positive in Case 1b, to weakly positive in Case 2b, and negative in Case 3b. This is a result of grains becoming more globular as the grain refiner level is increased from 0.2 kg/t to 20 kg/t and the dominant solute transport mechanism changes from liquid flow through the porous packed layer to grain settling. An illustration of the morphology transition can be seen in Figure 11d. The internal solid fraction across the cross-section of the ingot is plotted for Cases 1b, 2b, and 3b. We move from dendritic morphology for Case 1b ($g_{intern} \ll 1$) to globular morphology in Case 3b ($g_{intern} \sim 1$). Average equivalent grain sizes for all cases are reported in Table 5. Similarly as in the simulations with globular grains, the size of dendritic grains decreases with increasing grain refiner level. But for a given inoculant density, the model with globular morphology predicts lower grain size the model with dendritic morphology. This has been previously observed and reported by Heyvaert et al[40]. The predicted grain size variations across the ingot thickness were weak, of up to 10% in most of the ingot thickness and up to 25% in the vicinity of the ingot surface. Overall, the grain sizes predicted in this model are realistic and similar to sizes reported in Refs[11,41]. A more detailed discussion of grain size prediction in process-scale modeling of DC casting was presented recently by Bedel et al[42].

Thus, for the extreme case of grain refining (20 kg/t), the dendritic and the globular grain growth model converge and the differences between the models increase significantly as the grain refinement is reduced. This can be seen in the relative segregation profiles in Figure 11 (a,b,c). This preliminary study shows the close link between the morphology of the grain and the macroscopic transport mechanisms, which invariably affects the final macrosegregation in a DC cast ingot.

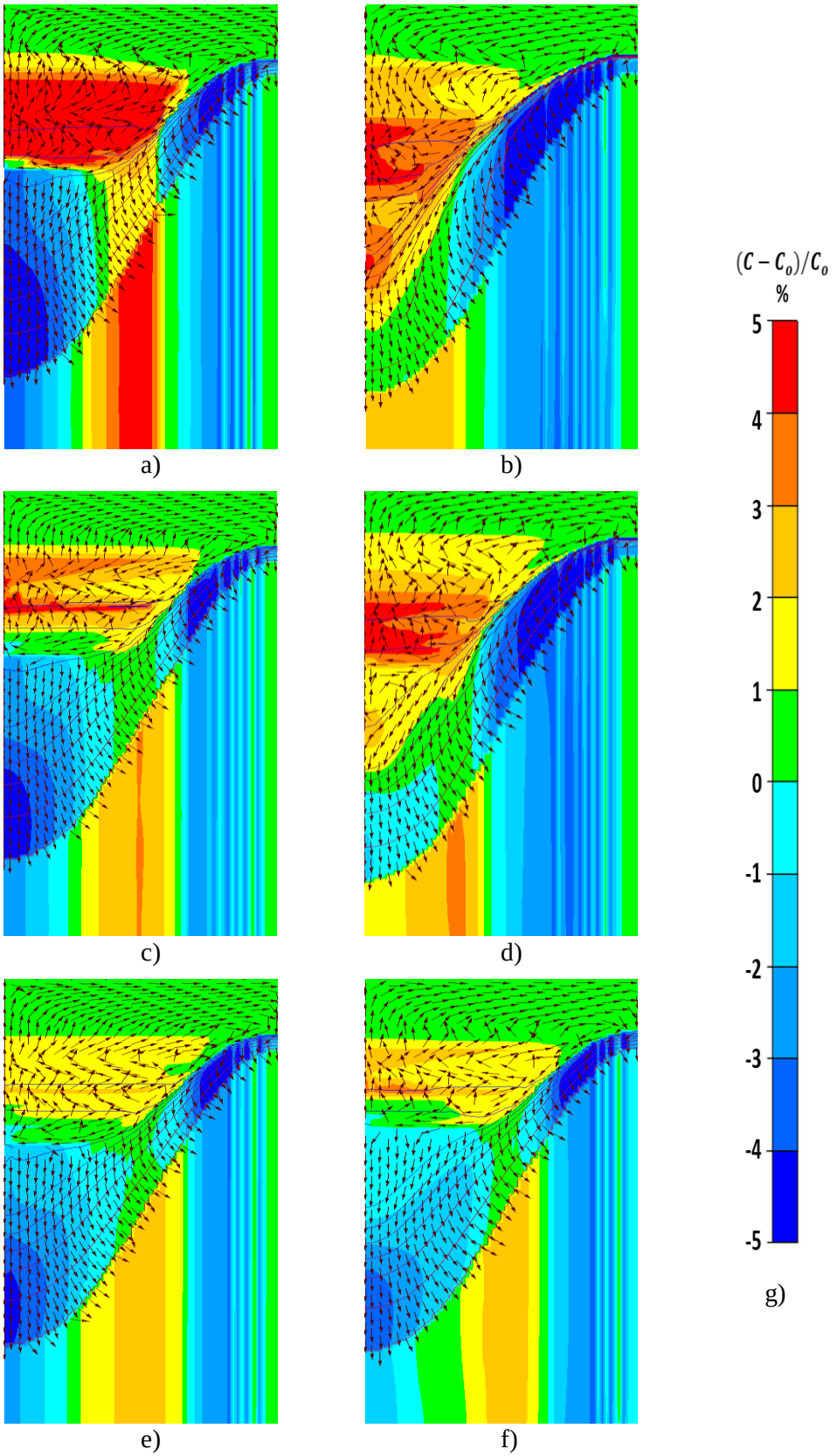

a) b) c) d) e) f) g)

Figure 10: Relative macrosegregation fields and isolines of envelope fraction overplotted with vectors of liquid relative velcity $\langle \vec{v}_l \rangle^l - \vec{V}_{cast}$ for different grain refiner levels. Globular morphology is imposed for a) Cases 1a, c) 2a, and e) 3a, morphology is calculated with the simplified three-phase model for b) Cases 1b, d) 2b, and f) 3b. g) The common color bar of relative macrosegregation for all cases.

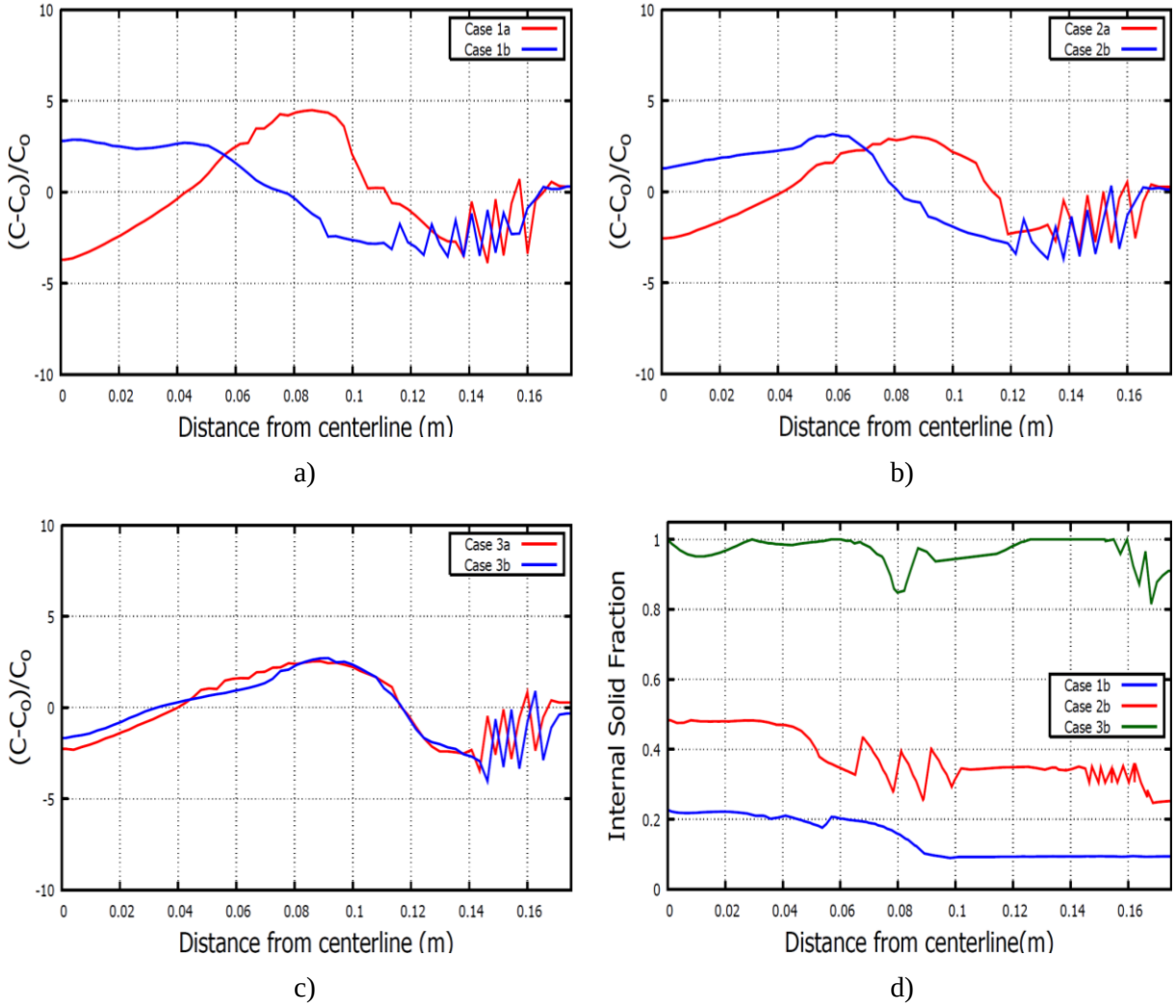

Figure 11: (a-c) Horizontal relative segregation profiles across the ingot for globular and dendritic growth models for different grain refiner levels, d) Horizontal profile of internal solid fraction for the cases simulated with the dendritic model.

5. Conclusions

A simplified formulation of a three-phase multiscale solidification model, in which macroscopic transport of heat, mass and momentum are coupled with microscopic grain nucleation and growth, accounting for morphology, was presented and the validity of model was assessed by comparing it with the full three phase model. The novelty of the proposed model formulation is the reduction of the number of coupled transport equations. Only three PDEs (for envelope volume, solid mass and solid concentration) instead of five (envelope volume, mass and concentrations for solid and intragranular liquid) need to be solved to describe the grain transport. This considerably reduces the computational cost as well as the complexity of implementation and of numerical solution of the model. It was shown

that the simplified model formulation is viable. The prediction of recalescence, important for coupling with nucleation models, is highly accurate. The simplified model gives somewhat more dendritic grain morphologies than the full model, but captures the morphology transition well.

The simplified model was then applied on an industrial sized DC cast ingot, accounting for grain motion, thermosolutal natural convection and shrinkage induced flow, to qualitatively study the impact of grain morphology on macrosegregation. The simulations indicate a strong link between grain morphology and macrosegregation. Grain morphology plays a key role in the macrosegregation formation due to its influence on grain settling and packing, and on intergranular liquid flow in the packed layer. The presented results suggest that a correct description of grain morphology is an important model ingredient to accurately predict negative segregation at the center of the ingot. Also, at higher grain density the model predicts a globularization of the morphology, similar to other results in the literature[38].

Although this model has been qualitatively tested on a DC cast case, a more rigorous experimental validation is necessary. Comparison of predicted grain structure and macrosegregation to experimental data can improve the confidence on this model and this will be the focus of future work.

Acknowledgement

This work is conducted within the framework of PRIMAL project with support from Hydro, Alcoa, Aleris, Research Council of Norway and NOTUR High Perfomance Computing program. M.Z. and H. C. acknowledge support by the French State through the program “Investment in the future” operated by the National Research Agency (ANR) and referenced by ANR-11 LABX-0008-01 (LabEx DAMAS).

6. References

1 R. Nadella, D.G. Eskin, Q. Du, and L. Katgerman: *Prog. Mater. Sci.*, 2008, vol. 53, pp. 421–80.
2 M. Rappaz and V. Voller: *Metall. Trans. A*, 1990, vol. 21, pp. 749–53.
3 W.D. Bennon and F.P. Incropera: *Int. J. Heat Mass Transf.*, 1987, vol. 30, pp. 2161–70.
4 V.R. Voller, A.D. Brent, and C. Prakash: *Int. J. Heat Mass Transf.*, 1989, vol. 32, pp. 1719–31.
5 A. V. Reddy and N.C. Beckermann: *Metall. Mater. Trans. B*, 1997, vol. 28, pp. 479–89.
6 T.. Finn, G. M.G, and W.D. Bennon: *ASME*, 1992, pp. 17–26.
7 Q. Du, D.G. Eskin, and L. Katgerman: *Metall. Mater. Trans. A Phys. Metall. Mater. Sci.*, 2007, vol. 38, pp. 180–9.
8 J. Ni and C. Beckermann: *Metall. Trans. B---Process Metall.*, 1991, vol. 22, pp. 349–61.
9 A. V. Reddy and C. Beckermann: *Mater. Process. Comput. Age II*, 1995, pp. 89–102.
10 L. Zhang, D.G. Eskin, A. Miroux, T. Subroto, and L. Katgerman: *IOP Conf. Ser. Mater. Sci. Eng.*, 2012, vol. 33, pp. 1–8.
11 L. Zhang, D.G. Eskin, A. Miroux, T. Subroto, and L. Katgerman: *Metall. Mater. Trans. B Process Metall. Mater. Process. Sci.*, 2012, pp. 1–9.
12 J. Li, M. Wu, A. Ludwig, and A. Kharicha: *Int. J. Heat Mass Transf.*, 2014, vol. 72, pp. 668–79.
13 M. Rappaz and P. Thévoz: *Acta Metall.*, 1987, vol. 35, pp. 1487–97.
14 M. Rappaz and P.H. Thévoz: *Acta Metall.*, 1987, vol. 35, pp. 2929–33.
15 P. Thévoz, J.L. Desbiolles, and M. Rappaz: *Metall. Trans. A*, 1989, vol. 20, pp. 311–22.
16 C.Y. Wang and C. Beckermann: *Metall. Mater. Trans. A*, 1996, vol. 27A, pp. 2754–64.
17 C.Y. Wang and C. Beckermann: *Metall. Mater. Trans. A*, 1996, vol. 27A, pp. 2765–83.
18 C.Y. Wang and C. Beckermann: *Metall. Trans. A*, 1993, vol. 24, pp. 2787–802.
19 M. Wu and A. Ludwig: *Acta Mater.*, 2009, vol. 57, pp. 5621–5631.
20 C.J. Vreeman and F.P. Incropera: *Int. J. Heat Mass Transf.*, 2000, vol. 43, pp. 677–86.

21 C.J. Vreeman and F.P. Incropera: *Int. J. Heat Mass Transf.*, 2000, vol. 43, pp. 687–704.
22 M. Založnik and H. Combeau: *Comput. Mater. Sci.*, 2010, vol. 48, pp. 1–10.
23 M. Založnik, A. Kumar, H. Combeau, M. Bedel, P. Jarry, and E. Waz: *Adv. Eng. Mater.*, 2011, vol. 13, pp. 570–80.
24 B. Appolaire, H. Combeau, and G. Lesoult: *Mater. Sci. Eng. A*, 2008, vol. 487, pp. 33–45.
25 M. Wu, A. Fjeld, and A. Ludwig: *Comput. Mater. Sci.*, 2010, vol. 50, pp. 32–42.
26 C.Y. Wang, S. Ahuja, C. Beckermann, and H.C. de Groh III: *Metall. Mater. Trans. B*, 1995, vol. 26, pp. 111–9.
27 H. Combeau, M. Založnik, S. Hans, and P.E. Richy: *Metall. Mater. Trans. B Process Metall. Mater. Process. Sci.*, 2009, vol. 40, pp. 289–304.
28 Ø. Nielsen, B. Appolaire, H. Combeau, and A. Mo: *Metall. Mater. Trans. A Phys. Metall. Mater. Sci.*, 2001, vol. 32, pp. 2049–60.
29 M. Rappaz and W.J. Boettinger: *Acta Mater.*, 1999, vol. 47, pp. 3205–19.
30 K.O. Tveito, M. Bedel, M. Založnik, H. Combeau, and M. M'Hamdi: *IOP Conf. Ser. Mater. Sci. Eng.*, 2012, vol. 27, p. 12040.
31 A.L. Greer, A.M. Bunn, A. Tronche, P. V. Evans, and D.J. Bristow: *Acta Mater.*, 2000, vol. 48, pp. 2823–35.
32 A. Tronche: PhD Thesis, University of Cambridge, Cambridge, England, 2000.
33 T.E. Quested: PhD Thesis, University of Cambridge, Cambridge UK, 2004.
34 D.A. Drew: *Ann. Rev. Fluid Mech*, 1983, vol. 15, pp. 261–91.
35 D. Weckman and P. Niessen: *Metall. Trans. B*, 1982, vol. 13, pp. 593–602.
36 M. Založnik, A. Kumar, H. Combeau, M. Bedel, P. Jarry, and E. Waz: *Essent. Readings Light Met. Vol. 3, Cast Shop Alum. Prod.*, 2013, pp. 848–53.
37 Ø. Nielsen, A. Mo, B. Appolaire, and H. Combeau: *Metall. Mater. Trans. A*, 2001, vol. 32, pp. 2049–60.
38 M. Založnik and H. Combeau: *Model. Cast. Weld. Adv. Solidif. Process. XII*, 2009, pp. 165–72.
39 H. Combeau, M. Založnik, and M. Bedel: *Jom*, 2016, vol. 68, pp. 2198–206.
40 L. Heyvaert, M. Bedel, M. Založnik, and H. Combeau: *Metall. Mater. Trans. A*, 2017, vol. 48, pp. 4713–34.
41 M. Bedel: PhD Theses Université de Lorraine, Nancy,France, 2010.
42 M. Bedel, L. Heyvaert, M. Založnik, H. Combeau, D. Daloz, and G. Lesoult: *IOP Conf. Ser. Mater. Sci. Eng.*, , DOI:10.1088/1757-899X/84/1/012100.